UKAEA-CCFE-PR(26)02

R. Martins, S. de Lara 1, J. B. Correia, A. Gonçalves,
A. Galatanu, D. Sobieraj, D. Nguyen-Manh, M. Dias1

(CrVW)(1-x)(TaTi)x, (x = 10 and 20 at.%), high entropy alloys as thermal barriers for nuclear fusion reactors

(CrVW)(1-x)(TaTi)x, (x = 10 and 20 at.%), high entropy alloys as thermal barriers for nuclear fusion reactors

R. Martins, S. de Lara 1, J. B. Correia, A. Gonçalves, A. Galatanu,
D. Sobieraj, D. Nguyen-Manh, M. Dias1

This is a preprint of a paper submitted for publication in
Journal of Nuclear Materials

$(CrVW)_{(1-x)}(TaTi)_x$, (x = 10 and 20 at.%), high entropy alloys as thermal barriers for nuclear fusion reactors

R. Martins [1], S. de Lara [1], J. B. Correia [2], A. Gonçalves [3],
A. Galatanu [4], D. Sobieraj[5], D. Nguyen-Manh[6,7], M. Dias[1]

[1] Instituto de Plasmas e Fusão Nuclear (IPFN), Instituto Superior Técnico, Universidade de Lisboa, Campus Tecnológico e Nuclear, Estrada Nacional 10, Bobadela, 2695-066, Portugal;
[2] Laboratório Nacional de Energia e Geologia (LNEG), Estrada do Paço do Lumiar, 1649-038 Lisboa, Portugal
[3] C2TN, Instituto Superior Técnico, Universidade de Lisboa, Campus Tecnológico e Nuclear, Estrada Nacional 10, 2695-066 Bobadela LRS, Portugal
[4] National Institute of Materials Physics, Atomistilor Street 405 A, Magurele, 077125 Ilfov, Romania
[5] Department of Materials Science and Engineering, Warsaw University of Technology, Woloska 141, Warsaw, 02-507, Poland
[6] Materials Division, United Kingdom Atomic Energy Authority Culham Campus, Abingdon, OX14 3DB, United Kingdom
[7] Department of Materials, University of Oxford, Parks Road, OX1 3PH, United Kingdom

CORRESPONDING AUTHOR:

Marta Dias

Instituto de Plasmas e Fusão Nuclear, Instituto Superior Técnico, Universidade de Lisboa, Av. Rovisco Pais, 1049-001, Lisboa, Portugal

Telephone: +351 21 9946051

Email: marta.dias@ctn.tecnico.ulisboa.pt

Graphical Abstract

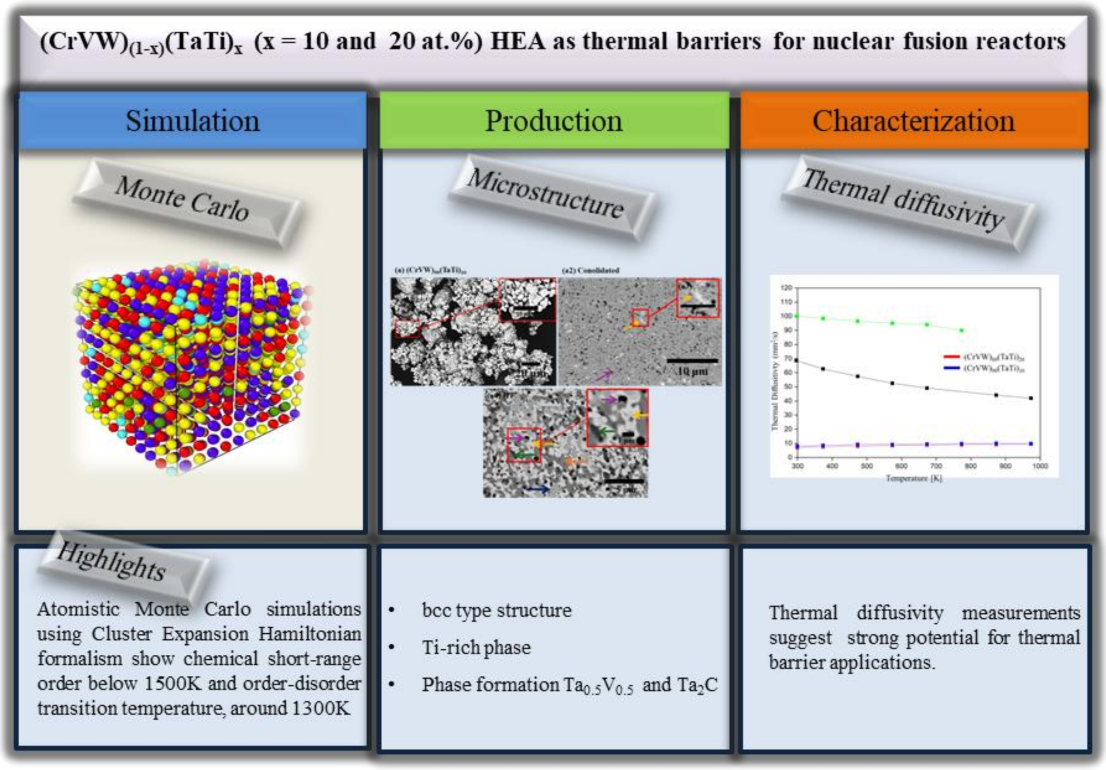

Abstract

Due to the extreme operating temperatures in nuclear fusion reactors, current materials exhibit a substantial mismatch in mechanical and thermal properties between the tungsten plasma-facing material and the CuCrZr heat sink cooling system. Therefore, a thermal barrier interlayer is required to guarantee continuous operation. In this work, $(CrVW)_{(1-x)}(TaTi)_x$ alloys, where (x = 10 and 20 at.%), were studied to be applied as interlayers. Atomistic modelling using Monte Carlo simulations combined with a first-principles-based Cluster Expansion Hamiltonian has been performed as a function of temperature to predict the order-disorder transitions for the investigated high entropy alloys. Moreover, the experimental alloys were prepared by mechanical alloying followed by spark plasma sintering. Both alloy compositions display strong negative average chemical short-range ordering below 1500 K for the W-Ta and W-Ti chemical pairs, with an estimated transition temperature) around 1300 K. Atomic structures obtained from Monte Carlo simulations for $(CrWV)_{80}(TaTi)_{20}$ indicate that the ordering observed here is stronger than that for $(CrWV)_{90}(TaTi)_{10.}$ Moreover, both systems display a bcc type structure, and heat treated samples exhibit phase growth and a microstructure with three phases. The thermal diffusivity values increase as the temperature rises, reaching low values compared to pure W and CuCrZr.

Keywords: molecular dynamics, high entropy alloys, Monte Carlo simulation, microstructure, X-ray diffraction.

1. Introduction

Nuclear fusion is a leading candidate for large-scale clean energy production, as it converts the energy released from fusion reactions into electrical energy [1]. Nevertheless, the materials used must be carefully chosen due to extreme temperatures and radiation. The divertor comprises plasma facing tungsten tiles [2][3], which collect the heat generated in operation and should operate at temperatures higher than 675 K [4]. This tends to lead to a high Ductile-to-Brittle Transition Temperature (DBTT) [4], which is a significant problem. Additionally, another challenge occurs when the heat sink CuCrZr alloy (chosen to remove heat [5][6]), which is attached to tungsten, must operate between 423 K and 623 K [5][6] due to the loss of mechanical properties at higher temperatures. Moreover, the different coefficients of thermal expansion (CTE), ($4.6x10^{-6}$/K) for tungsten and ($17.6x10^{-6}$/K) for CuCrZr [7][8][9], and the CuCrZr has a predisposition to suffer radiation damage that changes its mechanical properties [7][9][10], led to this material change. For this reason, an intermediate layer is required to minimize the mismatch between the plasma facing wall of W and the heat sink of CuCrZr, thereby prolonging the lifespan of the reactor and its materials [11].

In order to solve this issue, high entropy alloys research, especially on thermal and mechanical properties, has the potential to improve the performance and reliability of simulation models. High entropy alloys (HEAs) are advanced materials that exhibit exceptional thermal and mechanical properties, enabling them to withstand extreme environments [12][13]. Previous publications have shown that alloys with Ti, such as $(CrFeTaTi)_{70}W_{30}$ [14] and FeTiTaVW [15], revealed a complex microstructure with a Ti-rich phase. Titanium is a lightweight element with high strength and excellent oxidation resistance, which plays a crucial role in modifying the properties of high entropy alloys, contributing to their enhanced mechanical strength, corrosion resistance, and thermal stability. Chen, Yuhua, has shown that the addition of Ti in the $CoCrFeNiMnTi_x$ (x = 0, 0.25, and 0.55 mol%) alloy can change from a single fcc (Fe, Ni) phase to a bcc (Ti-rich) structure [16]. Titanium addition increased the material's hardness from 175 HV to 253 HV and 646 HV, respectively. As well as the tensile strength of the alloy is increased from 461 MPa to 631 MPa, along with Ti (x = 0 mol.% %) alloy to Ti (x = 0.25 mol. %) alloy, followed by a reduction to 287 MPa (x = 0.55 mol. %). Due to titanium's relatively large atomic radius, grain boundary segregation or clusters in multi-principal element systems can lead to microstructural inhomogeneity, affecting mechanical properties such as hardness and wear resistance. Therefore, the binary mixing enthalpy with Ti is significantly more negative than for the other possible atomic pairs, indicating that increasing the Ti concentration will inevitably result in a thermodynamic drive towards the formation of intermetallic phases, thereby decreasing the solid solution strengthening. In this way, a reduction of the amount of Ti is explored in this paper.

This work focuses on simulation, production, and characterization of the $(CrVW)_{(1-x)}(TaTi)_x$ where (x=10 and 20 at.%) high entropy alloy as a thermal barrier for nuclear reactors. With this in mind, the simulation behavior of $(CrVW)_{(90)}(TaTi)_{10}$ and $(CrVW)_{(80)}(TaTi)_{20}$, applying the first-principles thermodynamic approaches, including Density Functional Theory (DFT), Cluster Expansion (CE) method, will be employed [17][18]. A detailed insight into the formation and order-disorder stability of the two HEAs using Monte Carlo (MC) simulations for temperature-dependent properties will generate the atomistic structures and chemical short-range order parameters of each system [17][18]. In addition, $(CrVW)_{(1-x)}(TaTi)_x$ alloys (x = 10 and 20 at.%) were produced by mechanical alloying and then consolidated by spark plasma sintering (SPS). The bulk materials were characterized using Scanning Electron Microscopy (SEM), X-ray diffraction (XRD), and thermal diffusivity.

2. Experimental Details

In this study, Atomistic Monte Carlo (AMC) simulations were performed using Cluster Expansion Hamiltonian (CEH) formalism, which has been recently developed for studying the phase stability of compositionally complex and multicomponent systems as a function of temperature and irradiation damage for different W-based and Fe-based HEAs. The Cluster Expansion (CE) method can also be used to obtain the enthalpy of mixing values following the equation [17][18][19][20][21][22][23]:

$$\Delta H_{mix_{CE}}^{bcc}(\vec{\sigma}) = \sum_{\omega} m_{\omega} J_{\omega} \langle \Gamma_{\omega'}(\vec{\sigma}) \rangle_{\omega} \tag{1}$$

Where ω denotes clusters, the term m_ω represents the multiplicity factors, J_ω are effective cluster interactions derived from a set of DFT calculations applying the structure inversion approach and the term $\langle \Gamma_{\omega'}(\vec{\sigma}) \rangle$ stands for the average correlation functions. Cluster function can be described as follows:

$$\Gamma_{\omega,n}^{(s)}(\vec{\omega}) = \gamma_{j_1 K}(\sigma_1)\gamma_{j_2 K}(\sigma_2)\cdots\gamma_{j_{|\omega|}K}(\sigma_{|\omega|}) \tag{2}$$

Where $(s) = (j_1, j_2 \dots j_{|\omega|})$ denotes the pattern of assigning point functions to the cluster. Point functions $\gamma_{j,K}(\sigma_i)$ are then defined:

$$\gamma_{j,K}(\sigma_i) = \begin{cases} 1 & \text{if } j = 0 \\ -cos\left(2\pi \left\lceil \frac{j}{2} \right\rceil \frac{\sigma_i}{K}\right) & \text{if } j > 0 \text{ and odd} \\ -sin\left(2\pi \left\lceil \frac{j}{2} \right\rceil \frac{\sigma_i}{K}\right) & \text{if } j > 0 \text{ and even} \end{cases} \tag{3}$$

Where $\sigma_i = (0,1,2\ldots K - 1)$ denotes the index of the point function. The 2-body correlation functions are then defined as a product of pair probabilities in the following manner:

$$\left\langle \Gamma_{2,n}^{(s)} \right\rangle = \left\langle \Gamma_{2,n}^{ij} \right\rangle = \sum_{a=1}^{K} \sum_{b=1}^{K} \gamma_i(\sigma_a)\gamma_j(\sigma_b)y_n^{ab} \tag{4}$$

Where y_n^{ab} represents the probability of locating two atoms, *a* and *b*, within a specific shell, indicated by the label *n*. The 3-body correlation functions can be defined in a similar manner as follows:

$$\left\langle \Gamma_{3,n}^{(s)} \right\rangle = \left\langle \Gamma_{3,n}^{ijk} \right\rangle = \sum_{a=1}^{K} \sum_{b=1}^{K} \sum_{c=1}^{K} \gamma_i(\sigma_a)\gamma_j(\sigma_b)\gamma_k(\sigma_c)y_n^{abc} \tag{5}$$

Where y_n^{abc} represents the probability of locating three atoms, *a*, *b*, and *c*, within a specific shell, indicated by the label *n*. The Effective Cluster Interactions (ECIs) are obtained through a combination of DFT calculations and the Structure Inversion Method. First, DFT calculations are performed to determine the total energies of various configurations of atoms within a structure. These energies serve as a basis for deriving the interactions between clusters of atoms. The Structure Inversion Method is then applied to fit these calculated energies to a model that describes the interactions between clusters, extracting the ECIs. This approach enables the prediction of thermodynamic properties by accurately modeling interactions within the material's atomic arrangement. Canonical Exchange Monte Carlo (CEMC) is a simulation method used in computational statistical mechanics to study systems at constant temperature and constant particle number of each considered element. It is broadly used to investigate the phase transitions, structural changes, and thermodynamic properties of a given alloy composition. In this work, simulations were conducted by creating a fully disordered random configuration at 3000 K, then annealing it using the simulated annealing procedure with temperature steps of 10 K or 100 K. For each finite temperature, a series of exchanges involving neighboring atoms within the lattice was executed, and the resulting total energy of the system was calculated. If, as a result of such an exchange, the total energy has decreased, then the exchange of the atoms was accepted. In case the energy increased, the exchange was accepted with a probability defined as $e^{\left(-\frac{\Delta E}{k_B T}\right)}$. In the next step, the energy is averaged across all exchanges, and the newly updated atomic configuration transitions to the simulations at a different temperature. The Alloy Theoretic Automated Toolkit (ATAT) package, developed by van de Walle, Asta, and Ceder, was used to carry out MC simulations within this work [17][18][19][20][21][22][23].

Cr, V, Ta, Ti, and W powders of (99.9% nominal purity with an average particle size of 10 µm, AlfaAesar) were mixed in a non-equiatomic proportion $(CrVW)_{(1-x)}(TaTi)_x$, where x (x = 10 and 20 at.%). The systems were mechanically alloyed inside a high-energy planetary Restch EMAX milling equipment with 1 cm WC balls and WC vials. The balls-to-powder mass ratio was 10:1, and the milling occurred for 2 and 3 hours at 350 rpm.

X-ray diffraction measurements of the powder samples were performed at room temperature using monochromatic Cu Kα radiation in a Panalytical X´Pert Pro diffractometer with a 2θ–step size of 0.02º from 20º to 80º. The consolidation of the powders was done by Spark Plasma Sintering (SPS) in collaboration with Romania, using a FCT System Gmbh sintering machine at a pressure of 9 KN and a temperature of 1673 K (1400ºC) for a holding time of 5 minutes.

Metallographic preparation of the consolidated samples was performed by grinding with SiC paper, followed by polishing with diamond suspensions. The powders and sintered microstructures were observed using secondary electron (SE) and backscattered electron

(BSE) imaging in backscattering electron (BSE) mode with a Thermo Scientific Phenom ProX G6 scanning electron microscope, equipped with a 15 keV electron beam. Thermal treatments will be performed on a tubular furnace under vacuum at 1523K for 8 days to promote the growth of $(CrVW)_{90}(TaTi)_{10}$ and $(CrVW)_{80}(TaTi)_{20}$ phases. Moreover, the milled powder was analyzed using an analytical Empyrean diffractometer in reflection geometry, using Cu Kα1 radiation and a step size of 0.013 degrees.

Chemical information was obtained using X-ray energy-dispersive spectroscopy (EDS). Simple thermodynamic calculations were performed to anticipate the structures resulting from the alloying process and help interpret and discuss the results, based on empirical models [24][25]. In this context, calculations of the relevant properties of $(CrVW)_{(1-x)}(TaTi)_{x}$, where x = 10 and 20 at.%, are presented. The system $(CrVW)_{(1-x)}(TaTi)_{x}$ theoretical calculations are presented in Table 1.

Table 1 – Thermodynamic calculations for $(CrVW)_{90}(TaTi)_{10}$ and $(CrVW)_{80}(TaTi)_{20}$ systems.

Samples	ΔH_{mix} [kJ/mol]	ΔS_{mix} [J/K.mol]	δ [%]	VEC
$(CrVW)_{90}(TaTi)_{10}$	-2.51	13.25	4.63	5.55 (predicted bcc)
$(CrVW)_{80}(TaTi)_{20}$	-3.73	13.63	5.19	5.43 (predicted bcc)

3. Results and Discussion

3.1. Simulation results

In this study, Atomistic Monte Carlo (AMC) simulations were performed using the Cluster Expansion Hamiltonian (CEH) formalism, which has been recently developed to study the phase stability of compositionally complex and multi-component systems as a function of temperature in various multicomponent W-based alloys. As the temperature increases, the system undergoes a transition from ordered/segregated phases to a single solid solution phase. To quantitatively characterize this transition, the Warren-Cowley short-range order (SRO) parameter and the order-disorder transition temperature (ODTT) are introduced. The Warren-Cowley SRO parameter of atom types *i* and *j* can be calculated from pair probabilities [26][27]:

$$\alpha_n^{ij} = 1 - \frac{y_n^{ij}}{c_i c_j}. \qquad (11)(6)$$

In this equation, *n* denotes the n-th nearest neighbor, and y_n^{ij} is the probability to find the specific *i-j* pair in the n-th neighboring shell, which can be obtained by a matrix inversion of the correlation functions obtained from the CE, and c_i, c_j are the global concentration of atom types *i* and *j*. Here, we consider first and second nearest neighbors as well as the average (α_{avg}) SRO parameters in a BCC crystalline structure calculated as:

$$\alpha_{avg} = \frac{8\alpha_1 + 6\alpha_2}{14}, \qquad (12)(7)$$

A positive SRO parameter indicates a repulsive relationship between two different elements, while a negative SRO parameter indicates an attractive interaction. When the SRO parameter is zero, the system is in a random solid solution phase.

In Figure 1, the SRO values for first nearest neighbor (1NN) and second nearest neighbor (2NN), as well as the average of the chemical SRO parameter for the quinary $(CrWV)_{90}(TaTi)_{10}$ alloy, are presented as a function of temperature. It is shown that the SROs are negative for the chemical pairs W-Ta and W-Ti for both 1NN and 2NN, resulting in a strong negative average Chemical Short-Range Order (CSRO) below 1500 K.

It is observed that the Ta-Ti CSRO is more negatively pronounced than that between Cr-V for the alloys with low Ta and Ti compositions. Furthermore, V-Cr exhibits an average negative CSRO and a dominant positive SRO, with segregation between W-Cr, Ta-Cr, and Ta-V pairs. For the considered alloys, the average CSRO parameters between vanadium (V) and titanium (Ti) are positive.

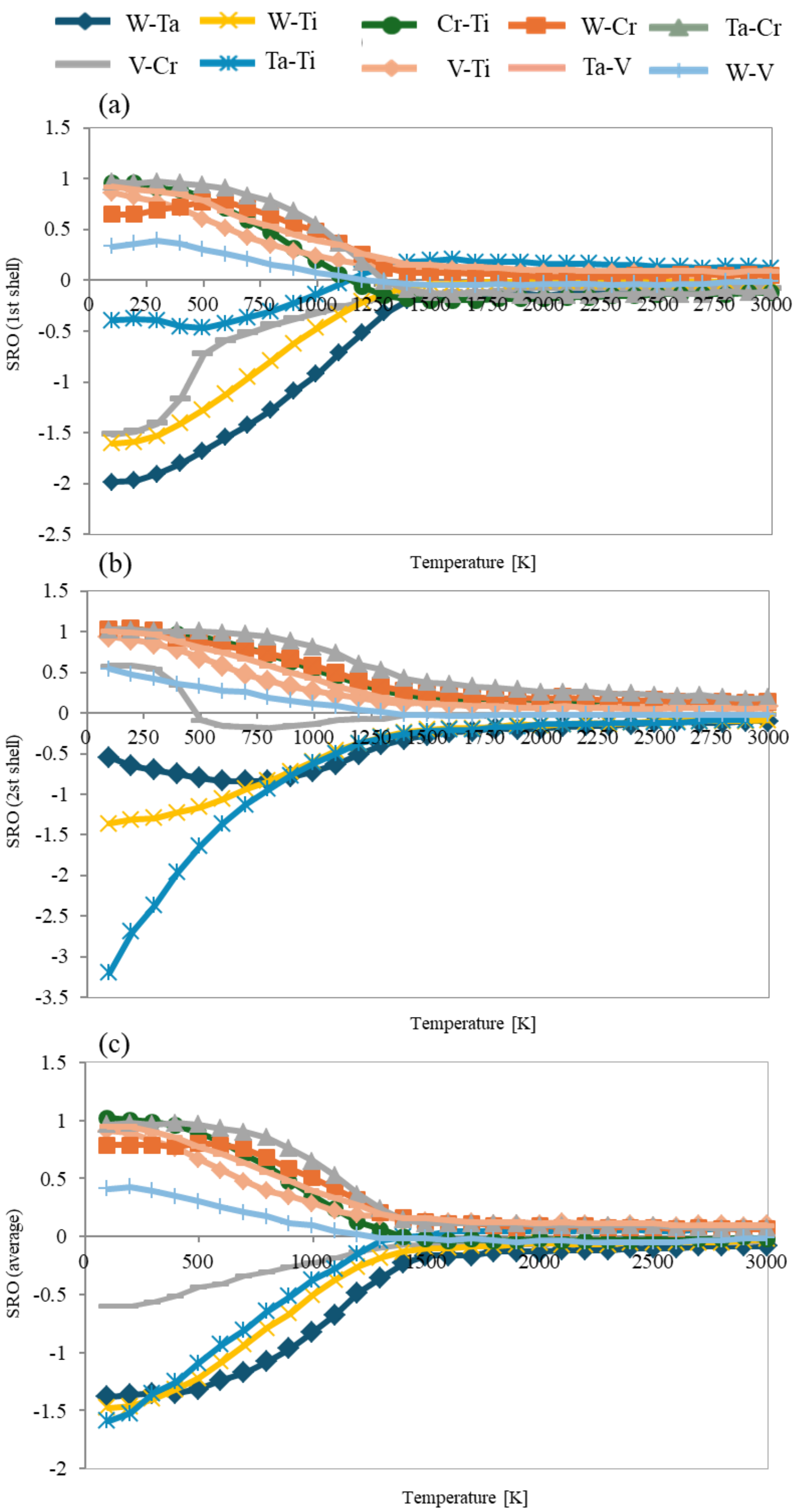

Figure 1- Chemical short-range order parameters obtained from Monte Carlo simulations as a function of temperature for the different pairs of atoms in (a) first nearest neighbor, (b) second nearest neighbor, and (c) average in the bcc lattice for $(CrWV)_{90}(TaTi)_{10}$ HEA.

Considering the definition of the order-disorder transition temperature (ODTT), this is defined as the temperature at which the alloy begins to become a fully disordered solid solution. In the present study, the highest temperature at which inflection points appear on the plot of enthalpy of mixing as a function of temperature is calculated for each composition. In Figure 2, the calculated enthalpy of mixing indicates that the ODTT for $(CrWV)_{90}(TaTi)_{10}$ is estimated to be around 1300 K.

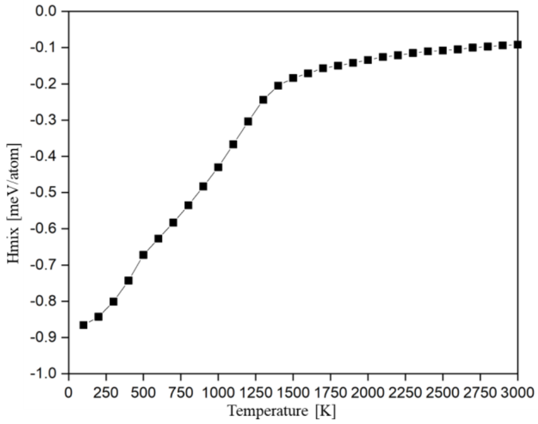

Figure 2 - Enthalpy of mixing as a function of temperature for $(CrWV)_{90}(TaTi)_{10}$.

Figure 3 shows the atomistic structures for $(CrWV)_{90}(TaTi)_{10}$ alloy obtained from Monte Carlo simulations as a function of temperature. Segregation between W atoms (yellow) from Cr atoms (blue) is observed at low temperatures (400 and 800 K). Starting from 1200 K, the stronger disordered configurations obtained are consistent with the predicted ODTT.

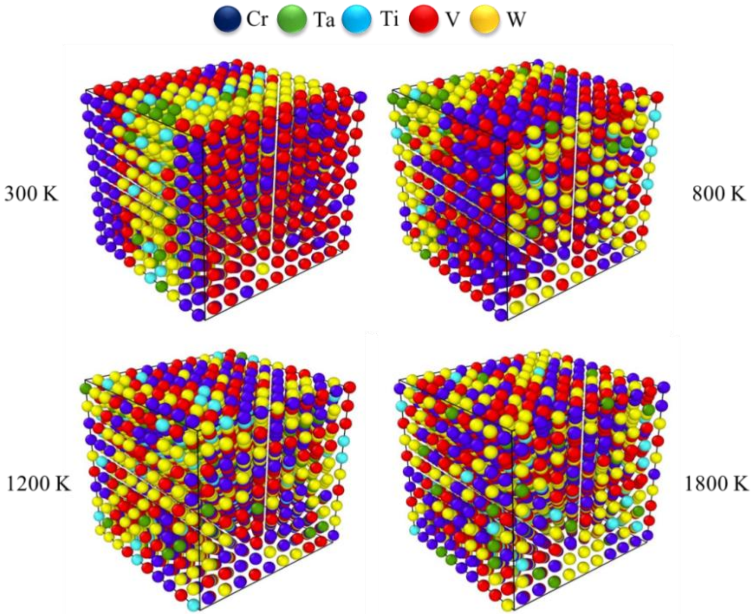

Figure 3- Atomic structures obtained from Monte Carlo simulations for a 10x10x10 bcc-supercell at four different temperatures: 400 K, 800 K, 1200 K, and 1800 K for $(CrWV)_{90}(TaTi)_{10}$.

Figures 4 (a) to (c) show the values for first nearest neighbor (1NN) and second nearest neighbor (2NN), for $(CrWV)_{80}(TaTi)_{20}$ alloy with increasing Ta and Ti concentrations and decreasing Cr, W, and V atomic concentration. The most significant change in CSRO compared to $(CrWV)_{90}(TaTi)_{10}$ is related to a weaker CSRO between Ta and Ti, whereas that between Cr and V becomes stronger, as exhibited in the average SRO values from Figure 4 (c).

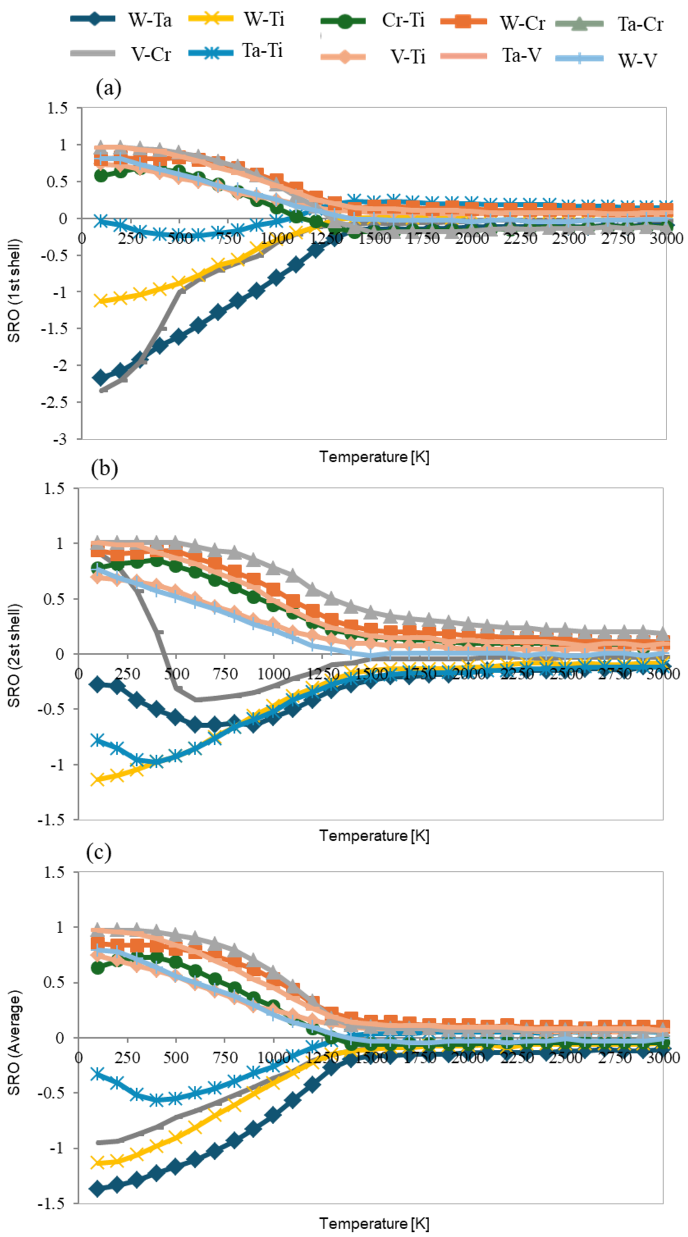

Figure 4 – Chemical short-range order parameters obtained from Monte Carlo simulations as a function of temperature for the different pairs of atoms in (a) first nearest neighbor, (b) second nearest neighbor, and (c) average in the bcc lattice for $(CrWV)_{80}(TaTi)_{20}$ HEA.

The competition between the SRO of Ta-Ti and those of Cr-V seems to result in an unchanging ODTT for $(CrWV)_{80}(TaTi)_{20}$. A comparison between the enthalpy of mixing is shown in Figure 5, which is similar to that in Figure 2.

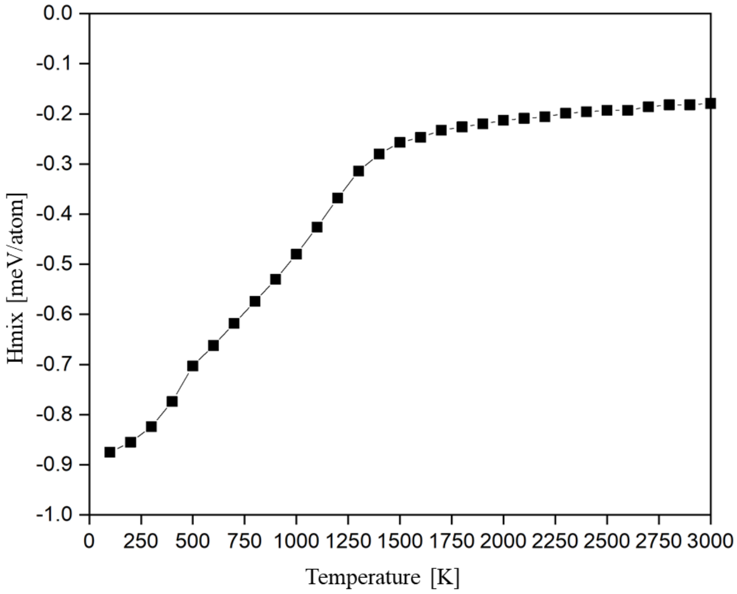

Figure 5 - Enthalpy of mixing as a function of temperature for $(CrWV)_{80}(TaTi)_{20}$.

However, the atomic structures obtained from Monte Carlo simulations at four different temperatures: 400 K, 800 K, 1200 K, and 1800 K for $(CrWV)_{80}(TaTi)_{20}$, shown in Figure 6, indicate that the ordering here is stronger than observed in a comparison with the case for $(CrWV)_{90}(TaTi)_{10}$.

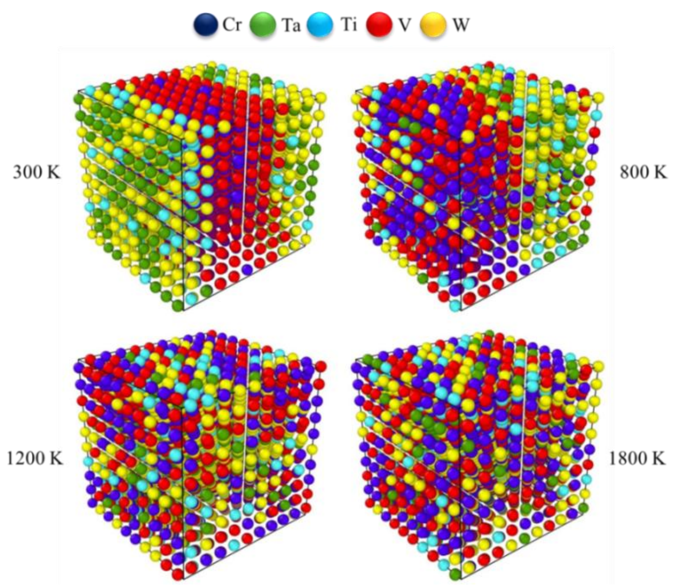

Figure 6 – Atomic structures obtained from Monte Carlo simulations for a 10x10x10 bcc-supercell at four different temperatures: 400 K, 800 K, 1200 K, and 1800 K for $(CrWV)_{80}(TaTi)_{20}$.

To cross-check the value of ODTT, larger Monte Carlo simulations were performed in HEAs with 30x30x30 bcc supercell sizes. The results are shown in Figure 7 for a comparison between the two investigated HEAs, $(CrWV)_{90}(TaTi)_{10}$ (top) and $(CrWV)_{80}(TaTi)_{20}$ (bottom), at three different temperatures: 400 K, 800 K, and 1200 K. It is now clearer that, in the thermodynamic limit, alloys with higher Ta and Ti concentrations exhibit a more substantial segregation effect, reflecting the driving force between W and Cr. It can be concluded that the ODTT (around 1400 K) is higher in $(CrWV)_{80}(TaTi)_{20}$ compared to $(CrWV)_{90}(TaTi)_{10}$.

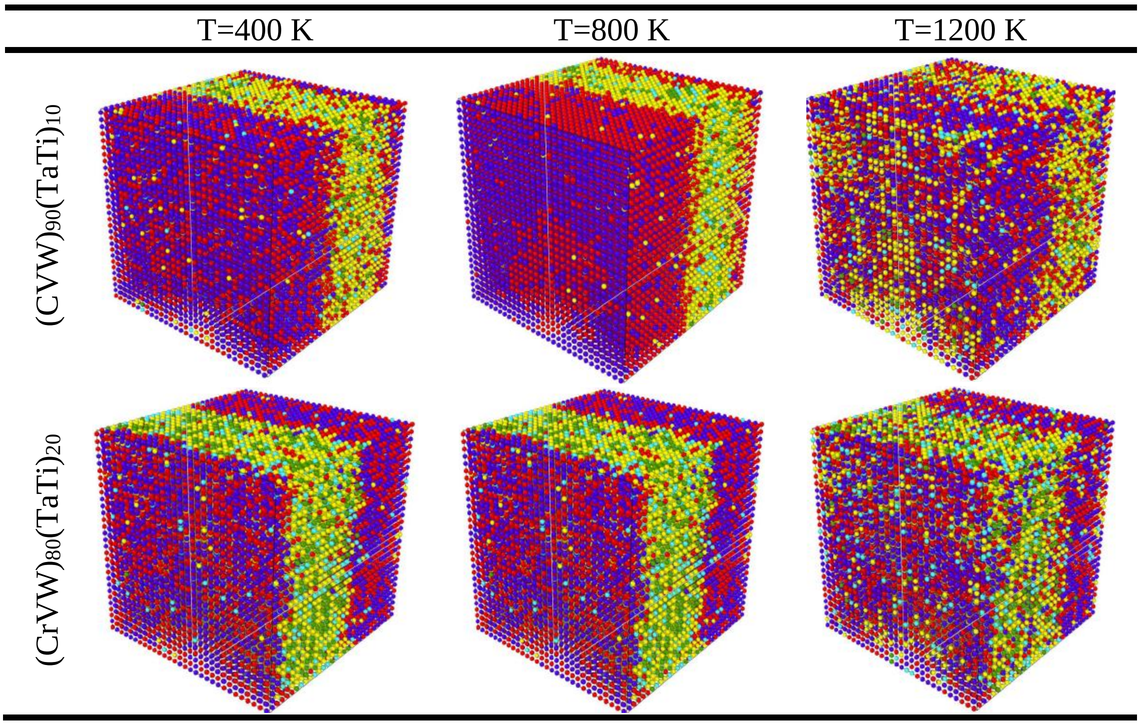

Figure 7 - Larger scale (30x30x30 bcc supercell) Monte Carlo simulation results at three temperatures (400 K, 800 K, and 1200 K) for $(CrWV)_{90}(TaTi)_{10}$ (top) and $(CrWV)_{80}(TaTi)_{20}$ (down) HEAs.

3.2. Powder characterization

Figure 8 (a1) and (b1) show the experimental diffractograms for (a) $(CrVW)_{90}(TaTi)_{10}$ and (b) $(CrVW)_{80}(TaTi)_{20}$ initial powder without milling. After two hours of milling, Figures 8 (a2) and (b2), the individual peaks of the elements disappeared, and a bcc type structure with a lattice parameter of a = 0.316 nm, displaying a lattice parameter very close to that of pure W (a = 0.316 nm [28]), formed.

Additionally, the presence of pure tantalum and chromium with low intensity is also observed (identified by the black diamond and black triangle symbols), as shown in Figures 8 (a2) and (b2), respectively. In addition, some weak peaks corresponding to WC are also observed, indicating the presence of WC in the material due to the use of WC grinding balls in the mechanical alloying process. Since pure Ta and Cr were detected after two hours of milling, the powders were milled for an additional hour at 350 rpm to promote a single solid solution. After a total of 3 hours of milling, as shown in Figures 8 (a3) and (b3), the experimental diffractogram displayed a bcc type peak with a lattice parameter of a = 0.315 nm for both the $(CrVW)_{90}(TaTi)_{10}$ and $(CrVW)_{80}(TaTi)_{20}$ systems, respectively. The WC peaks are still observed, while the peaks for pure tantalum and chromium have disappeared.

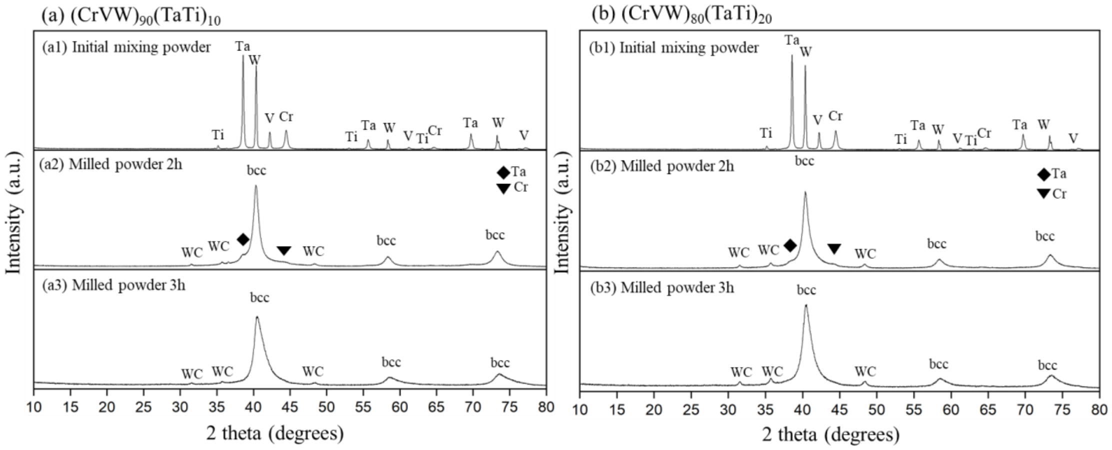

Figure 8 - Experimental diffractograms for $(CrVW)_{90}(TaTi)_{10}$ and (d) $(CrVW)_{80}(TaTi)_{20}$ compositions. Experimental diffractograms for (a1) and (b1) the initial powder mixture, (a2) and (b2) the milled powders after 2 hours of mechanical alloying at 350 rpm, and (a3) and (b3) the milled powders after a total of 3 hours of mechanical alloying at 350 rpm.

Figure 9 shows the morphology for the milled (a) $(CrVW)_{90}$ $(TiTa)_{10}$ and (b) $(CrVW)_{80}(TiTa)_{20}$ powders, as well as the respective EDS maps. These two compositions were milled by the mechanical alloying process for 3 hours. Figure 9 (a1) and (b1) revealed that the milled powders for both compositions consist of small particles agglomerated with larger ones. Figure 9 (a2) to (a6) and (b2) to (b6) exhibits the EDS maps for both systems, showing that all elements for both compositions are very well mixed and display a homogeneous distribution, in agreement with the experimental diffractograms bcc type structures shown in Figure 8 (a3) and (b3).

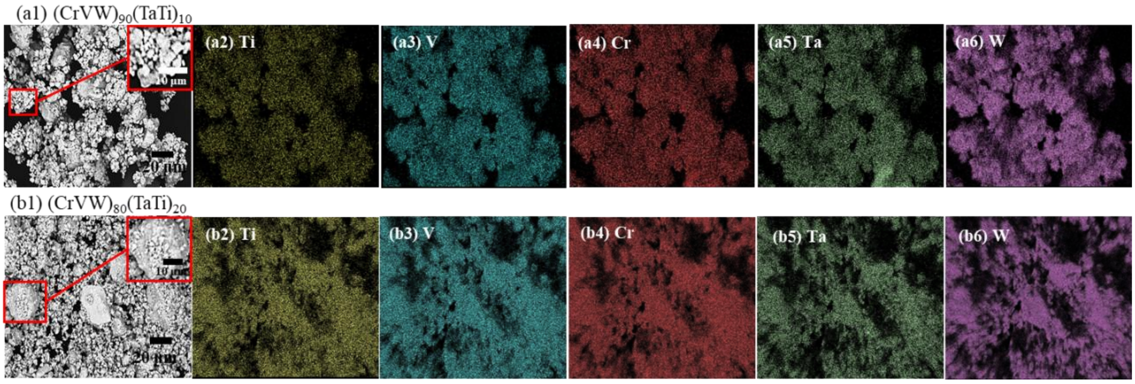

Figure 9 - BSE images of the milled powders of (a) $(CrVW)_{90}(TiTa)_{10}$ and (b) $(CrVW)_{80}(TiTa)_{20}$ compositions, together with EDS maps for (a2) and (b2) Ti-Kα, (a3) and (b3) V-Kα, (a4) and (b4) Cr-Kα, (a5) and (b5) Ta-Lα, and (a6) and (b6) W-Lα X-ray lines.

3.3. Consolidated samples characterization

The $(CrVW)_{90}(TiTa)_{10}$ diffractogram shown in Figure 10 (a) exhibits a bcc type structure that exhibits a lattice parameter of a = 0.305 nm. Additionally, it displays peaks with similar intensity associated with the intermetallic $Ta_{0.5}V_{0.5}$, which has a bcc type structure and exhibits a lattice parameter of a = 0.317 nm, as well as the CdI_2-PbI_2 polytype carbide Ta_2C phase. The presence of such carbides was observed in similar high entropy alloys, WTaTiVCr [29], produced under the same conditions as the materials presented in this paper, with identical lattice parameters. This similarity may be attributed to the use of graphite dies in the sintering process. Figure 10 (b) exhibits the experimental diffractogram for the $(CrVW)_{80}(TiTa)_{20}$ sample. A bcc type structure is observed on the diffractogram exhibiting the highest intensity peak with a lattice parameter of a = 0.307 nm. Additionally, another bcc type structure (identified with a black star) displays a lattice parameter of a = 0.317 nm and corresponds to an intermetallic $Ta_{0.5}V_{0.5}$ with a bcc type structure. Moreover, peaks (identified with a black circle and black diamonds) corresponding to CdI_2-PbI_2 polytype simulated carbide (Ta_2C) and an unidentified peak, respectively, are also identified.

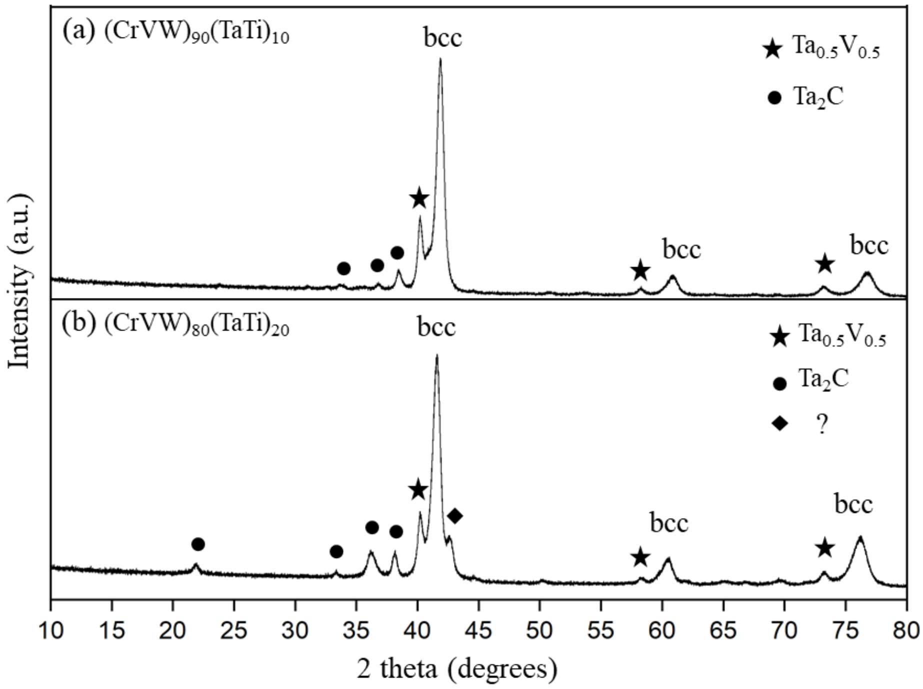

Figure 10 - Experimental diffractograms for (a) $(CrVW)_{90}(TaTi)_{10}$ and (d) $(CrVW)_{80}(TaTi)_{20}$ compositions. A black star and circle indicate the presence of $Ta_{0.5}V_{0.5}$, and Ta_2C, respectively. Black diamonds indicate the presence of an unidentified peak.

The $(CrVW)_{90}$(TaTi a)$_{10}$ microstructure is shown in Figure 11, featuring a nanometric microstructure with black spots and a major phase containing some small particles. The sample densities were measured, displaying densification higher than 98%. No porosity was observed in the microstructure, corroborating the high densification values. Figures 11 (b) to (f) show the EDS maps for the $(CrVW)_{90}(TaTi)_{10}$ sample, indicating an almost homogeneous distribution of all elements as well as an extremely fine microstructure. The dark areas in Figures 11 (a) and (b) point to a titanium-rich phase. In contrast, the small light areas correspond to tungsten-rich regions in Figures 11 (a) and (f). Moreover, Figure 12 displays the SEM images and EDS maps for the $(CrVW)_{80}(TaTi)_{20}$ sample, which shows a microstructure similar to that of $(CrVW)_{90}(TaTi)_{10}$. Due to the nanometric microstructure, it is extremely difficult to characterize the phases present in both samples.

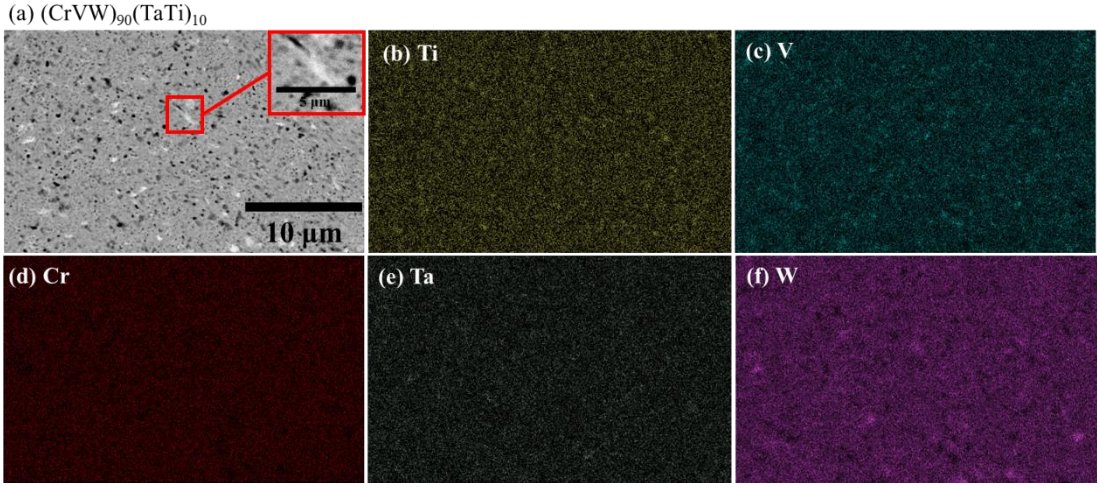

Figure 11 - (a) SEM images of the samples (a) consolidated spark plasma sintering $(CrVW)_{90}(TaTi)_{10}$ sample. EDS maps for (b) Ti-Kα, (c) Cr-Kα, (d) Ta, Lα, and (e) W-Lα X-ray lines.

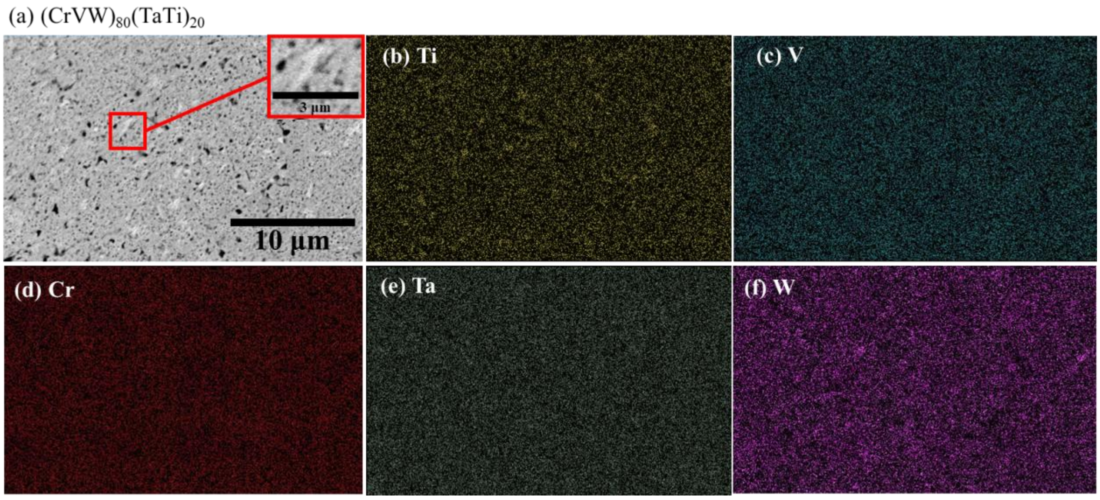

Figure 12 - (a) SEM images of the samples (a) consolidated spark plasma sintering $(CrVW)_{80}(TaTi)_{20}$ sample. EDS maps (b) Ti-Kα, (c) Cr-Kα, (d) Ta, Lα, and (e) W-Lα X-ray lines.

Due to the fine microstructures of the alloys, a heat treatment was performed on $(CrVW)_{90}(TaTi)_{10}$ and $(CrVW)_{80}(TaTi)_{20}$ in a tubular furnace under vacuum at 1523K for 8 days. The experimental diffractogram of the annealed $(CrVW)_{90}(TaTi)_{10}$ alloy is shown in Figure 13 (a), which demonstrates the appearance of a bcc-type structure with a lattice parameter of a =0.312 nm (presented as bcc_1). It exhibits a minor bcc-type structure with a lattice parameter of a = 0.296 nm (presented as bcc_2). Also, it is possible to observe the presence of non-identified weak peaks indicated as a black diamond in Figure 13 (a). The experimental diffractogram of the annealed $(CrVW)_{80}(TaTi)_{20}$, shown in Figure 13 (b), exhibits the appearance of a bcc-type structure with a lattice parameter of a = 0.311 nm. The presence of the Laves phase (identified by a black square) confirms the presence of intermetallic phases after heat treatment.

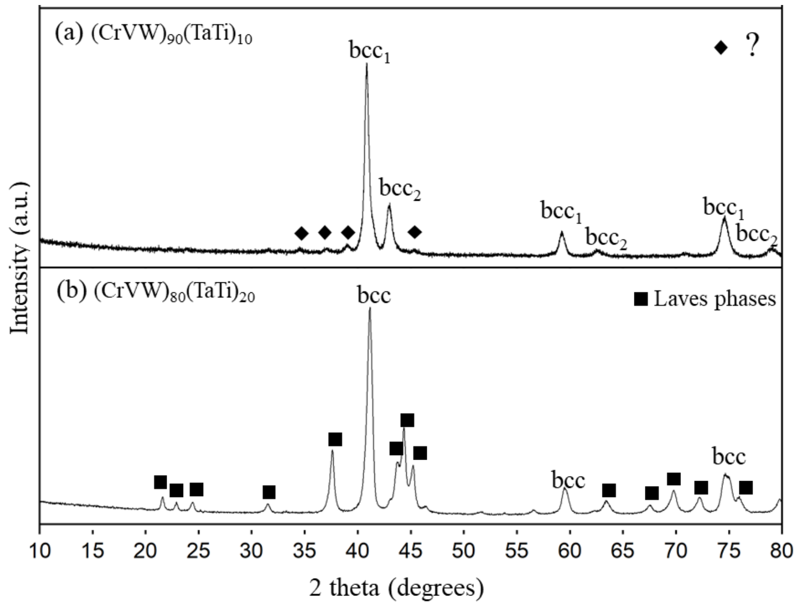

Figure 13 - Experimental diffractograms for annealed (a) $(CrVW)_{90}(TaTi)_{10}$ samples and (d) annealed $(CrVW)_{80}(TaTi)_{20}$ samples. Black diamond indicates the presence of unknown phases, and the black square indicates the presence of the laves phase.

Figure 14 (a) shows the SEM image of the heat treated $(CrVW)_{90}(TaTi)_{10}$ sample, revealing microstructural grain growth and displaying the presence of multiple distinct phases. This growth is created by diffusion between the elements, which generated the present phases. Nevertheless, the microstructure still displays a nanometric microstructure. Five phases were identified: a darker phase, three intermediate phases, and a lighter phase. The darker phases (indicated by the purple arrow in Figures 14 (a) and (b)) correspond to a Ti-rich phase. The intermediate phases correspond to V, Ta, and Cr-rich phases (indicated by the green, blue, and orange arrows in Figure 14 (c), (d), and (e)), and the light phase corresponds to the W-rich areas (indicated by the yellow arrow in Figure 14 (a) and (f)). A similar microstructure was observed in the $(CrVW)_{80}(TaTi)_{20}$ composition shown in Figure 15. However, upon examining the microstructure, Ta, Cr, and V appear to be more evenly distributed. The Laves phase simulated was $Fe_2Ta_{0.5}W_{0.5}$, a C14 phase with an hcp type structure (hexagonal close-packed). The samples produced in this work do not have Fe, and no simulated CrTaW intermetallic was found [30]. However, the structure of $Fe_2Ta_{0.5}W_{0.5}$ seems to fit well in the X-ray pattern of $(CrVW)_{80}(TaTi)_{20}$. Hence, the only possibility is replacing the element Fe with Cr, due to their similar atomic radius. The appearance of Laves phases is very typical in alloys with elements with a specific difference in atomic size, especially during SPS and subsequent annealing at elevated temperatures. Larry Kaufman [31] studied the thermodynamics of the Cr-Ta-W system by combining the Ab Initio and CALPHAD methods, demonstrating the possibility of C14 laves phases in the Cr-Ta-W system. Other articles hint at the formation of AB_2 stoichiometry Laves phase occurrence, where A is a large atom (Ti, Zr, Hf, Nb, Ta) and B is a small atom (V, Mo, W, Fe, Cr, Co) [32][33].

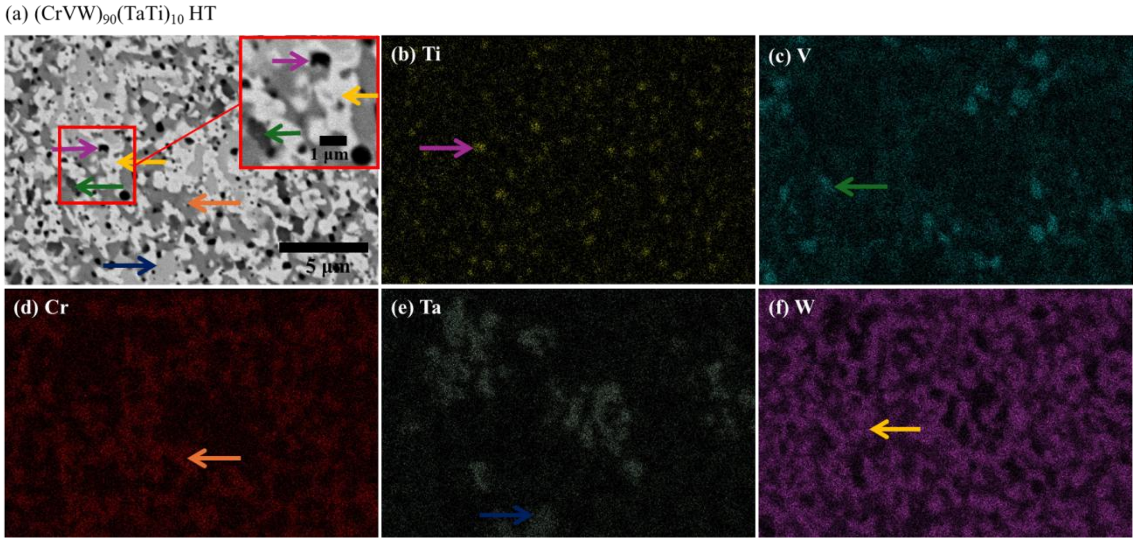

Figure 14 - (a) SEM images of the samples (a) consolidated annealed spark plasma sintering $(CrVW)_{90}(TaTi)_{10}$ sample. EDS maps for Ti-Kα, (c) Cr-Kα, (d) Ta-Lα, and (e) W-Lα X-ray lines

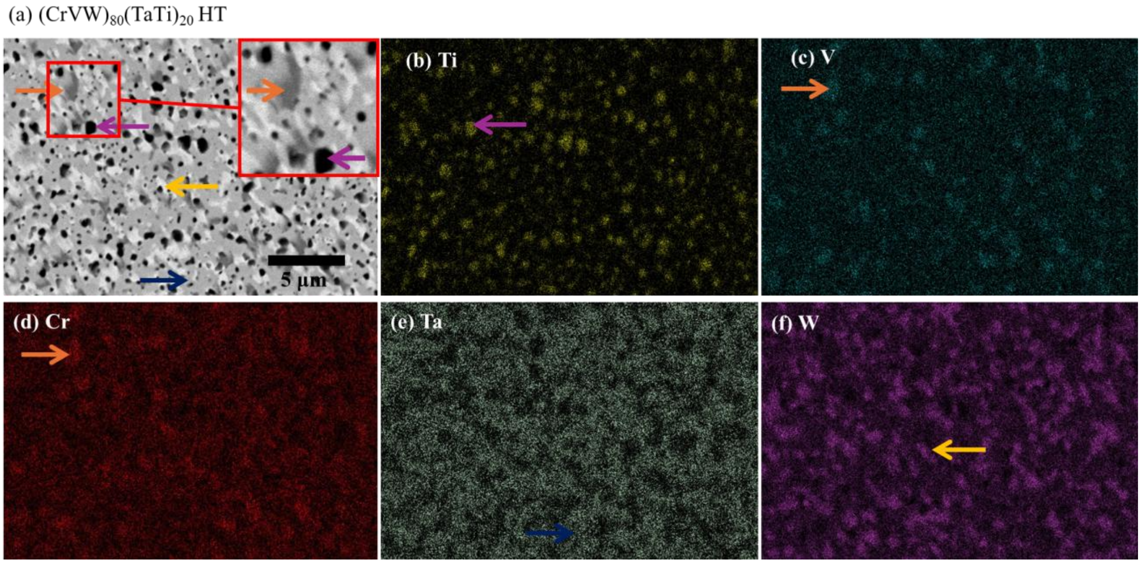

Figure 15 - (a) SEM images of the samples (a) consolidated annealed spark plasma sintering $(CrVW)_{80}(TaTi)_{20}$ sample. EDS maps for (b) Ti-Kα, (c) Cr-Kα, (d) Ta-Lα, Lα, and (e) W-Lα X-ray lines.

It is worth nothing that most diffusion studies on high entropy alloys focus on fcc type structures due to their relatively well-characterized and straightforward nature, which results in low lattice distortion and lattice strain [35][41][42]. In contrast, body centered cubic structures can exhibit significant distortions and higher lattice strain, which strongly influence diffusion behavior [43][44]. Before heat treatment, both alloys exhibited nanometric microstructures that were difficult to characterize. However, post heat treatment analysis revealed apparent differences in phase evolution. The $(CrVW)_{90}(TaTi)_{10}$ alloy developed five distinct phases (Figure 14), while the $(CrVW)_{80}(TaTi)_{20}$ alloy, shown in Figure 15, displayed only three. However, there are small Cr- and V-rich areas that create an intermediate, darker phase (identified with the orange arrow in Figures 15 (a), (c), and (d)). Since both samples were heat treated under the same conditions, this disparity suggests that the $(TaTi)_{10}$ composition promoted the formation of a new phase when compared with the $(TaTi)_{20}$ one. Tantalum and titanium have atomic radii of 0.143 nm and 0.146 nm, respectively, which are significantly larger than those of Cr, V, and W. As a result, increasing the (TaTi) content and decreasing (CrVW) concentrations led to a higher atomic size difference (δ), rising from 4.6 in $(CrVW)_{90}(TaTi)_{10}$ to 5.6 for $(CrVW)_{80}(TaTi)_{20}$. This increase likely contributes to the so-called sluggish diffusion effect, a characteristic often attributed to HEAs. This phenomenon is driven by complex and disordered local bonding environments that elevate activation energies for atomic migration, thereby slowing diffusion. Consequently, the higher Ta and Ti content is expected to suppress phase formation by hindering atomic mobility. Our results support this: the alloy with greater δ exhibited fewer phases after heat treatment, indicating a higher degree of sluggish diffusion, which aligns with the experimental results. This could stem from a combination of mass disorder, increased lattice strain, and/or altered local structural dynamics. Razumovsky [35] noted that different diffusion mechanisms vary among elements. While Ta, Nb, Mo, and Hf primarily diffuse via the vacancy mechanism, Zr and Ti diffuse through the much faster interstitial mechanism.

Furthermore, simulation results indicate that W-Ta and W-Ti exhibit a strong negative CSRO below 1500 K, suggesting a higher probability of segregation. Considering that the ODTT is around 1300 K, the consolidated temperature at 1673 K might not be sufficient to promote complete diffusion of the elements into the microstructure. This incomplete diffusion process may also contribute to the formation of phases and/or intermetallic compounds. In addition, simulation results show that increasing Ta and Ti concentrations and decreasing Cr, W, and V concentrations lead to a significant change in CSRO between $(CrWV)_{90}(TaTi)_{10}$ and $(CrWV)_{80}(TaTi)_{20}$. A weaker CSRO simulated between Ta and Ti observed in $(CrWV)_{80}(TaTi)_{20}$, together with a stronger Cr and V bonding pair, could lead to the formation of the three phases microstructure on this system, while the $(CrWV)_{90}(TaTi)_{10}$ HEA exhibits a stronger Ta and Ti CSRO and a weaker Cr and V bonding pair, which could lead to the formation of a microstructure with five phases. Although these phenomena are interesting, they require further characterization to be conclusive.

3.4. Thermal diffusivity

Figure 16 illustrates the thermal diffusivity of the $(CrWV)_{80}(TaTi)_{20}$ and $(CrWV)_{90}(TaTi)_{10}$ high-entropy alloys over the range of 300 to 1000 K. Both samples exhibit a similar thermal diffusivity behavior as a function of temperature, with diffusivity values increasing as the temperature rises, reaching values between 7 mm^2/s and 9 mm^2/s. The $(CrWV)_{90}(TaTi)_{10}$ exhibits slightly higher thermal diffusivity values than $(CrWV)_{80}(TaTi)_{20}$. Compared to pure tungsten [45] and CuCrZr [46][47], both $(CrWV)_{80}(TaTi)_{20}$ and $(CrWV)_{90}(TaTi)_{10}$ high entropy alloys demonstrate significantly lower diffusivity values. As proposed by the author in [50], the enhanced thermal diffusivity observed at higher temperatures in HEAs is attributed to lattice dilation, which lengthens the phonon mean free path as temperature rises. In high entropy alloys, the phonon mean free path is short due to atomic-level disorder, resulting in high phonon scattering rates. Tantalum and titanium have atomic radii of 0.143 nm and 0.1462 nm, respectively, which are significantly larger than those of Cr, V, and W. As a result, increasing the (TaTi) content and decreasing (CrVW) concentrations led to a higher atomic size difference (δ), leading to the small changes in thermal diffusivity observed.HEA works like VFeTiTaW [15], $(CrFeTaTi)_{70}W_{30}$ [14], as well as $W_{57}Ta_{21}V_{11}Ti_{8}Cr_{3}$ alloys [49] report similar thermal diffusivity values at elevated temperatures, in the range of 3 to 10 mm^2/s.

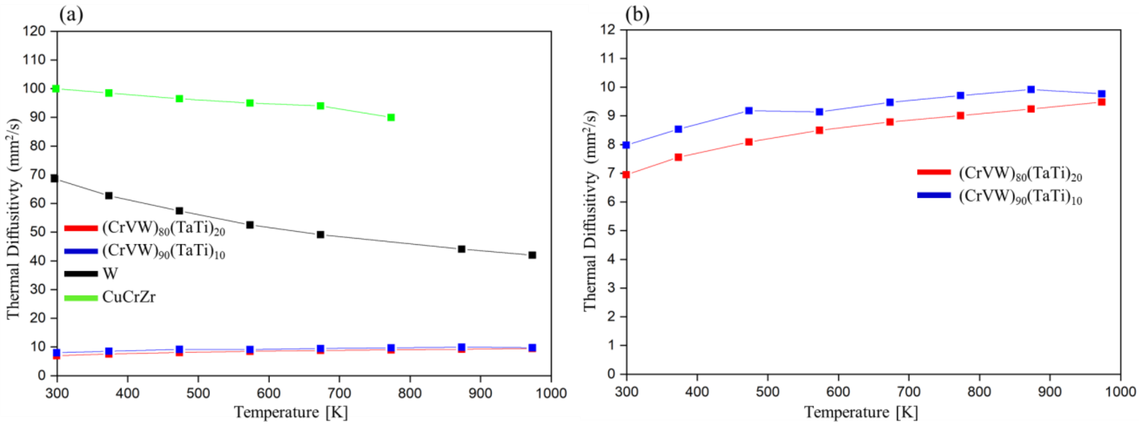

Figure 16 - Thermal diffusivity of $(CrVW)_{90}(TaTi)_{10}$ and $(CrVW)_{90}(TaTi)_{10}$ consolidated sample together with pure W [51], and CuCrZr [46][47].

4. Conclusions

This study investigated the structural evolution of the high entropy alloys $(CrVW)_{90}(TaTi)_{10}$ and $(CrVW)_{80}(TaTi)_{20}$ systems as potential thermal barriers to reduce the mismatch between tungsten plasma facing components and CuCrZr heat sinks in nuclear fusion divertors.

Atomistic simulations showed temperature-dependent bonding and segregation trends up to 1500 K, with preferential bonding between W–Ta and W–Ti chemical pairs. The chemical short-range order (CSRO) and order-disorder transition temperature (ODTT) provide important insights into the bonding strength between all elements, leading to the conclusion that increasing Ta and Ti concentration will result in a comparable microstructure at lower temperatures. This is supported by the thermodynamic ODTT limit, which shows that the alloys with higher Ta and Ti concentrations exhibit a more substantial segregation effect, reflecting the driving force between W and Cr at higher temperatures.

SEM images of both systems revealed a nanometric microstructure after sintering. Due to grain growth following annealing, the microstructure evolved into a $(CrVW)_{80}(TaTi)_{20}$ with three phases and a $(CrVW)_{90}(TaTi)_{10}$ with five phases. After annealing treatment, it is evident that $(CrVW)_{90}(TaTi)_{10}$ exhibits a lower sluggish diffusion effect compared to $(CrVW)_{80}(TaTi)_{20}$. This is an occurrence reinforced due to the difference in atomic size (δ), rising from 4.6 in $(CrVW)_{90}(TaTi)_{10}$ to 5.6 for

$(CrVW)_{80}(TaTi)_{20}$, and a significant change in CSRO values between (Ta and Ti) and (Cr and V) exhibited amongst $(CrWV)_{90}(TaTi)_{10}$ and $(CrWV)_{80}(TaTi)_{20}$. The thermal diffusivity values increase as the temperature rises, reaching values between 7 mm^2/s and 9 mm^2/s for both $(CrVW)_{90}(TaTi)_{10}$ and $(CrVW)_{80}(TaTi)_{20}$. These values are well within the range of other known HEA values. Overall, the simulations underscore the crucial role of computational modeling in elucidating phase stability and atomic interactions of each element in HEAs. Further characterization, particularly through transmission electron microscopy (TEM) or atomic probe tomography (APT), should be performed to provide additional information and lay the groundwork for future investigations into their functional and mechanical properties.

Acknowledgments

This work has been carried out within the framework of the EUROfusion Consortium, funded by the European Union via the Euratom Research and Training Programme (Grant Agreement No 101052200 — EUROfusion). Views and opinions expressed are, however, those of the author(s) only and do not necessarily reflect those of the European Union or the European Commission. Neither the European Union nor the European Commission can be held responsible for them. IPFN activities were supported by FCT - Fundação para a Ciência e Tecnologia, I.P. by project reference UID/50010/2023, UID/PRR/50010/2025 and by project reference LA/P/0061/2020

5. References

[1] C.-J. Tong *et al.*, "Mechanical performance of the Al x CoCrCuFeNi high-entropy alloy system with multiprincipal elements," *Metall. Mater. Trans. A*, vol. 36, no. 5, pp. 1263–1271, May 2005, doi: 10.1007/s11661-005-0218-9.

[2] "ITER." Accessed: Sep. 09, 2022. [Online]. Available: https://www.iter.org/proj/inafewlines#4

[3] J. N. Brooks *et al.*, "Plasma-surface interaction issues of an all-metal ITER," *Nucl. Fusion*, vol. 49, no. 3, 2009, doi: 10.1088/0029-5515/49/3/035007.

[4] P. M. Raole and S. P. Deshpande, "Structural materials for fusion reactors," *Trans. Indian Inst. Met.*, vol. 62, no. 2, pp. 105–111, 2009, doi: 10.1007/s12666-009-0014-0.

[5] V. Barabash *et al.*, "Materials challenges for ITER - Current status and future activities," *J. Nucl. Mater.*, vol. 367-370 A, no. SPEC. ISS., pp. 21–32, 2007,

doi: 10.1016/j.jnucmat.2007.03.017.
[6] V. Barabash *et al.*, “Materials challenges for ITER - Current status and future activities,” *J. Nucl. Mater.*, vol. 367-370 A, no. SPEC. ISS., pp. 21–32, 2007, doi: 10.1016/j.jnucmat.2007.03.017.
[7] T. R. Barrett *et al.*, “Enhancing the DEMO divertor target by interlayer engineering,” *Fusion Eng. Des.*, vol. 98–99, pp. 1216–1220, 2015, doi: 10.1016/j.fusengdes.2015.03.031.
[8] J. H. You *et al.*, “European DEMO divertor target: Operational requirements and material-design interface,” *Nucl. Mater. Energy*, vol. 9, pp. 171–176, 2016, doi: 10.1016/j.nme.2016.02.005.
[9] A. J. Cackett, H. T. Vo, J. J. H. Lim, A. J. Bushby, P. Hosemann, and C. D. Hardie, “Effects of radiation damage and precipitate distribution on micro-pillar compression testing of irradiated CuCrZr,” *J. Nucl. Mater.*, vol. 553, 2021, doi: 10.1016/j.jnucmat.2021.153028.
[10] O. V. Ogorodnikova, B. Tyburska, V. K. Alimov, and K. Ertl, “The influence of radiation damage on the plasma-induced deuterium retention in self-implanted tungsten,” *J. Nucl. Mater.*, vol. 415, no. 1 SUPPL, pp. S661–S666, 2011, doi: 10.1016/j.jnucmat.2010.12.012.
[11] P.-K. Huang, J.-W. Yeh, T.-T. Shun, and S.-K. Chen, “Multi-Principal-Element Alloys with Improved Oxidation and Wear Resistance for Thermal Spray Coating,” *Adv. Eng. Mater.*, vol. 6, no. 12, pp. 74–78, Feb. 2004, doi: 10.1002/adem.200300507.
[12] I. Toda-Caraballo and P. E. J. Rivera-Díaz-Del-Castillo, “A criterion for the formation of high entropy alloys based on lattice distortion,” *Intermetallics*, vol. 71, pp. 76–87, 2016, doi: 10.1016/j.intermet.2015.12.011.
[13] J.-W. Yeh, “Recent progress in high-entropy alloys,” *Eur. J. Control - EUR J Control*, vol. 31, pp. 633–648, Dec. 2006, doi: 10.3166/acsm.31.633-648.
[14] R. Martins *et al.*, “Influence of Cr on the quaternary FeTaTiW medium entropy alloy,” *J. Mater. Sci. Mater. Eng.*, vol. 20, no. 1, pp. 1–13, 2025, doi: 10.1186/s40712-025-00256-1.
[15] R. Martins *et al.*, “Simulation , Structural , Thermal and Mechanical Properties of the FeTiTaVW High Entropy Alloy,” 2024.
[16] Y. Chen *et al.*, “Effect of Ti Content on the Microstructure and Properties of CoCrFeNiMnTix High Entropy Alloy,” *Entropy*, vol. 24, no. 2, pp. 1–11, 2022, doi: 10.3390/e24020241.
[17] B. Sun *et al.*, “Thermodynamic assessment of the quaternary WTaCrV refractory high entropy alloy as a means to guide experimental approaches,” *Acta Mater.*, vol. 299, no. August, p. 121435, 2025, doi: 10.1016/j.actamat.2025.121435.
[18] A. Fernández-Caballero, J. S. Wróbel, P. M. Mummery, and D. Nguyen-Manh, “Short-Range Order in High Entropy Alloys: Theoretical Formulation and Application to Mo-Nb-Ta-V-W System,” *J. Phase Equilibria Diffus.*, vol. 38, no. 4, pp. 391–403, 2017, doi: 10.1007/s11669-017-0582-3.
[19] F. R. A. N. C. O. I. . Ducastelle, *Order and phase stability in alloys. Interatomic Potential and Structural Stability*. Springer Berlin Heidelberg, 1993. doi: 10.1007/978-3-642-84968-8_14.
[20] Q. Wu, B. He, T. Song, J. Gao, and S. Shi, “Cluster expansion method and its application in computational materials science,” *Comput. Mater. Sci.*, vol. 125, pp. 243–254, 2016, doi: 10.1016/j.commatsci.2016.08.034.
[21] R. Chinnappan, B. K. Panigrahi, and A. van de Walle, “First-principles study of phase equilibrium in Ti–V, Ti–Nb, and Ti–Ta alloys,” *Calphad Comput.*

Coupling Phase Diagrams Thermochem., vol. 54, pp. 125–133, 2016, doi: 10.1016/j.calphad.2016.07.001.
[22] J. M. Sanchez, “Foundations and Practical Implementations of the Cluster Expansion,” *J. Phase Equilibria Diffus.*, vol. 38, no. 3, pp. 238–251, 2017, doi: 10.1007/s11669-017-0521-3.
[23] J. M. Sanchez, F. Ducastelle, and D. Gratias, “Generalized cluster description of multicomponent systems,” *Phys. A Stat. Mech. its Appl.*, vol. 128, no. 1–2, pp. 334–350, 1984, doi: 10.1016/0378-4371(84)90096-7.
[24] S. Guo and C. T. Liu, “Phase stability in high entropy alloys: Formation of solid-solution phase or amorphous phase,” *Prog. Nat. Sci. Mater. Int.*, vol. 21, no. 6, pp. 433–446, 2011, doi: 10.1016/S1002-0071(12)60080-X.
[25] Y. Zhang, Y. J. Zhou, J. P. Lin, G. L. Chen, and P. K. Liaw, “Solid-solution phase formation rules for multicomponent alloys,” *Adv. Eng. Mater.*, vol. 10, no. 6, pp. 534–538, 2008, doi: 10.1002/adem.200700240.
[26] B. E. Warren, *X-ray diffraction*. Dover Publications, 1990.
[27] J. M. Cowley, “An approximate theory of order in alloys,” *Phys. Rev.*, vol. 77, no. 5, pp. 669–675, 1950, doi: 10.1103/PhysRev.77.669.
[28] X. Qi, N. Cai, T. Chen, S. Wang, and B. Li, “Experimental and theoretical studies on the elasticity of tungsten to 13 GPa,” *J. Appl. Phys.*, vol. 124, no. 7, 2018, doi: 10.1063/1.5044519.
[29] S. Alvi, O. A. Waseem, and F. Akhtar, “High temperature performance of spark plasma sintered w0.5(tativcr)0.5 alloy,” *Metals (Basel).*, vol. 10, no. 11, pp. 1–12, 2020, doi: 10.3390/met10111512.
[30] W. B. P. P. Villars, K. Cenzual, “Pearson’s crystal data : crystal structure database for inorganic compounds,” *Chem. Mater. Sci.*, 2007.
[31] L. Kaufman, P. E. A. Turchi, W. Huang, and Z. K. Liu, “Thermodynamics of the Cr-Ta-W system by combining the Ab Initio and CALPHAD methods,” *Zentropy Tools, Model. Appl.*, vol. 25, no. 3, pp. 51–72, 2001, doi: 10.1201/9781003514466-3.
[32] F. Zareipour, H. Shahmir, and Y. Huang, “Formation and significance of topologically close-packed Laves phases in refractory high-entropy alloys,” *J. Alloys Compd.*, vol. 986, no. September 2023, p. 174148, 2024, doi: 10.1016/j.jallcom.2024.174148.
[33] B. S. Murty, J. W. Yeh, S. Ranganathan, and P. P. Bhattacharjee, “Special subgroups of high-entropy alloys,” *High-Entropy Alloy.*, pp. 145–163, 2019, doi: 10.1016/b978-0-12-816067-1.00008-4.
[34] D. Ni, “Experimental investigations on the quinary interdiffusivities in diffusion couples of NiAlCoCr alloy / CoCrFeNi high-entropy alloys,” *Calphad*, vol. 76, no. October 2021, p. 102388, 2022, doi: 10.1016/j.calphad.2021.102388.
[35] J. Dąbrowa, W. Kucza, G. Cieślak, T. Kulik, M. Danielewski, and J. W. Yeh, “Interdiffusion in the FCC-structured Al-Co-Cr-Fe-Ni high entropy alloys: Experimental studies and numerical simulations,” *J. Alloys Compd.*, vol. 674, pp. 455–462, 2016, doi: 10.1016/j.jallcom.2016.03.046.
[36] V. Verma, A. Tripathi, and K. N. Kulkarni, “On Interdiffusion in FeNiCoCrMn High Entropy Alloy,” *J. Phase Equilibria Diffus.*, vol. 38, no. 4, pp. 445–456, 2017, doi: 10.1007/s11669-017-0579-y.
[37] K. Kulkarni and G. P. S. Chauhan, “Investigations of quaternary interdiffusion in a constituent system of high entropy alloys,” *AIP Adv.*, vol. 5, no. 9, 2015, doi: 10.1063/1.4931806.
[38] K. Y. Tsai, M. H. Tsai, and J. W. Yeh, “Sluggish diffusion in Co-Cr-Fe-Mn-Ni

high-entropy alloys," *Acta Mater.*, vol. 61, no. 13, pp. 4887–4897, 2013, doi: 10.1016/j.actamat.2013.04.058.

[39] A. Mehta and Y. Sohn, "Investigation of sluggish diffusion in FCC Al0.25CoCrFeNi high-entropy alloy," *Mater. Res. Lett.*, vol. 9, no. 5, pp. 239–246, 2021, doi: 10.1080/21663831.2021.1878475.

[40] M. Vaidya, S. Trubel, B. S. Murty, G. Wilde, and S. V. Divinski, "Ni tracer diffusion in CoCrFeNi and CoCrFeMnNi high entropy alloys," *J. Alloys Compd.*, vol. 688, no. October 2017, pp. 994–1001, 2016, doi: 10.1016/j.jallcom.2016.07.239.

[41] J. Dąbrowa and M. Danielewski, "State-of-the-art diffusion studies in the high entropy alloys," *Metals (Basel).*, vol. 10, no. 3, 2020, doi: 10.3390/met10030347.

[42] M. S. Daw and M. Chandross, "Sluggish diffusion in random equimolar FCC alloys," *Phys. Rev. Mater.*, vol. 5, no. 4, p. 43603, 2021, doi: 10.1103/PhysRevMaterials.5.043603.

[43] S. V. Divinski, A. V. Pokoev, N. Esakkiraja, and A. Paul, "A Mystery of 'Sluggish Diffusion' in High-Entropy Alloys: The Truth or a Myth?," *Diffus. Found.*, vol. 17, pp. 69–104, 2018, doi: 10.4028/www.scientific.net/df.17.69.

[44] M. I. Razumovsky, B. S. Bokstein, A. O. Rodin, and A. V. Khvan, "Interdiffusion in Refractory Metal System with a BCC Lattice: Ti/TiZrHfNbTaMo," *Entropy*, vol. 25, no. 3, pp. 1–22, 2023, doi: 10.3390/e25030490.

[45] C. Pradère, J. M. Goyhénèche, J. C. Batsale, S. Dilhaire, and R. Pailler, "Thermal diffusivity measurements on a single fiber with microscale diameter at very high temperature," *Int. J. Therm. Sci.*, vol. 45, no. 5, pp. 443–451, 2006, doi: 10.1016/j.ijthermalsci.2005.05.010.

[46] M. Rohde *et al.*, "Intercomparison of thermal diffusivity measurements on CuCrZr and PMMA," *High Temp. - High Press.*, vol. 42, no. 6, pp. 469–474, 2014.

[47] F. M. Copper, "CuCr1Zr," 2024.

[48] K. Jin *et al.*, "Thermophysical properties of Ni-containing single-phase concentrated solid solution alloys," *Mater. Des.*, vol. 117, pp. 185–192, 2017, doi: 10.1016/j.matdes.2016.12.079.

[49] Y. Li *et al.*, "Preliminary exploration of a WTaVTiCr high-entropy alloy as a plasma-facing material," *Nucl. Fusion*, vol. 62, no. 12, 2022, doi: 10.1088/1741-4326/ac8fa5.

[50] C. L. Lu, S. Y. Lu, J. W. Yeh, and W. K. Hsu, "Thermal expansion and enhanced heat transfer in high-entropy alloys," *J. Appl. Crystallogr.*, vol. 46, no. 3, pp. 736–739, 2013, doi: 10.1107/S0021889813005785.

[51] B. Hay *et al.*, "Uncertainty Assessment for Very High Temperature Thermal Diffusivity Measurements on Molybdenum, Tungsten and Isotropic Graphite," *Int. J. Thermophys.*, vol. 43, no. 1, 2022, doi: 10.1007/s10765-021-02926-6.